Sub-Volt High-Speed Silicon MOSCAP Microring Modulator Driven by High Mobility Conductive Oxide

Wei-Che Hsu[1,2], Nabila Nujhat[1], Benjamin Kupp[1], John F. Conley, Jr[1], Haisheng Rong[3], Ranjeet Kumar[3], and Alan X. Wang[1,2,*]

[1]School of Electrical Engineering and Computer Science, Oregon State University, Corvallis, Oregon 97331, USA

[2]Department of Electrical and Computer Engineering, Baylor University, One Bear Place #97356, Waco, Texas 76798, USA

[3]Intel Corporation, 3600 Juliette Ln, Santa Clara, CA 95054

[*]alan_wang@baylor.edu

ABSTRACT

Low driving voltage (V_{pp}), high-speed silicon microring modulator plays a critical role in energy-efficient optical interconnect and optical computing systems owing to its ultra-compact footprint and capability for on-chip wavelength-division multiplexing. However, existing silicon microring modulators usually require more than 2 V of V_{pp}, which is limited by the relatively weak plasma dispersion effect of silicon and the small capacitance density of the reversed PN-junction. Here we present a highly efficient metal-oxide semiconductor capacitor (MOSCAP) microring modulator through heterogeneous integration between silicon photonics and titanium-doped indium oxide, which is a high-mobility transparent conductive oxide (TCO) material with a strong plasma dispersion effect. The device is co-fabricated by Intel's photonics fab and TCO patterning processes at Oregon State University, which exhibits a high electro-optic modulation efficiency of 117 pm/V with a low V_{π}•L of 0.12 V•cm, and consequently can be driven by an extremely low V_{pp} of 0.8 V. At a 11 GHz modulation bandwidth where the modulator is limited by the high parasitic capacitance, we obtained 25 Gb/s clear eye diagrams with energy efficiency of 53 fJ/bit and demonstrated 35 Gb/s open eyes with a higher driving voltage. Further optimization of the device is expected to increase the modulation bandwidth up to 52 GHz that can encode data at 100 Gb/s for next-generation, energy-efficient optical communication and computation with sub-volt driving voltage without using any high voltage swing amplifier.

Introduction

Optical microring resonators have emerged as a key building block of photonic integrated circuits (PICs) that can function as versatile optical devices including modulators, wavelength filters and multiplexers, in comb lasers, weight banks for neuromorphic computing, and optical sensors[1–3]. They are playing increasingly critical roles in optical communication, optical interconnects, optical computing, and biomedical sensing due to their ultra-compact footprint and capability for on-chip wavelength-division multiplexing (WDM)[4]. Although optical microring resonators have been implemented on various platforms such as thin-film $LiNbO_3$[5], silicon nitride[6], and plasmonics[7], active silicon microring modulators (Si-MRMs) that can perform high-speed electro-optic (E-O) modulation as the photonic engine for future PICs remains as the climax of research[8–10]. Silicon photonics provides a mature, cost-effective platform to integrate Si-MRMs with lasers, photodetectors, passive optical devices, and even microelectronic circuits through standard foundry fabrication, which is still the only feasible solution to build large-scale PICs with both active and passive devices for complex systems[11,12].

Existing Si-MRMs available in the foundry process are based on reversed PN junctions, which can achieve ultra-high modulation bandwidth but usually require more than 2 V of driving voltage (V_{pp})[13–16]. Such high V_{pp} is induced by the relatively weak plasma dispersion effect of silicon and the small capacitance per unit length of the reversed PN-junction, which is usually less than 2 fF/μm[17,18]. The high V_{pp} makes it unfeasible to drive Si-MRMs directly by CMOS logic circuits. For example, today's 5nm CMOS has a core supply of 0.65 V and input/output supply of 1 V[19]. Therefore, high voltage-swing CMOS transmitter (TX) circuits that consume hundreds of milliwatts of power must be used to drive the Si-MRMs. For instance, the 106 Gb/s 2.5 Vpp Si-MRM driver using 28nm CMOS process consumes 1.33 pJ/bit energy with Pulse-amplitude modulation 4-level (PAM-4) while the Si-MRM itself usually consumes less than 100 fJ/bit energy[20]. As a comparison, MOSCAP-driven Si-MRMs can achieve a much larger capacitance density using ultra-thin high dielectric constant insulators such as HfO_2. In addition, MOSCAP devices allow heterogeneous integration of more E-O efficient gate materials with Si waveguide such as III-V compound semiconductors and graphene[21–28]. In the past two decades, high-speed MOSCAP Si-MRMs, including heterogeneously integrated functional materials, have been demonstrated (Supplementary Information I)[7,10,29–33]. Nevertheless, a high-speed Si-MRM with sub-volt V_{pp} and large E-O modulation efficiency has not been reported.

In this article, we demonstrate a highly efficient MOSCAP Si-MRM heterogeneously integrated with titanium-doped indium oxide (ITiO), a TCO with high carrier mobility. The focus of this study is to achieve sub-volt V_{pp} modulation with a high E-O bandwidth, which requires optimization of the quality factor (Q-factor) and the E-O efficiency of the MRM. A higher Q-factor allows for narrower resonant spectra, enabling lower V_{pp}. However, it

also leads to a longer photon lifetime, which imposes a limitation on the modulation bandwidth. Therefore, enhancing the E-O efficiency of the MRM through other mechanisms using more efficient gate material and higher capacitance density becomes crucial. The ITiO-gated MOSCAP Si-MRM in this work achieved a high E-O efficiency of 117 pm/V with a V_{π}•L of 0.12 V•cm by narrowing the microring waveguide width to 300 nm, which effectively improved the overlapping factor between the accumulated carriers and the optical mode profile[34]. The utilization of high mobility ITiO reduces the optical waveguide absorption, enabling a moderate Q-factor of 4600 for sub-volt V_{pp} modulation while still supporting a photon lifetime-limited bandwidth up to 50 GHz. Additionally, the high mobility ITiO, along with optimized doping on the Si microring waveguide and metal electrode patterning, improved the RC bandwidth significantly compared with all previous work[35,36]. As a result, the ITiO-gated MOSCAP Si-MRM can be driven by 0.8 V_{pp} with 11 GHz E-O bandwidth, demonstrating a clear eye diagram at 25 Gb/s with energy efficiency of 53 fJ/bit and 35 Gb/s open eyes with a V_{pp} of 1.75 V after de-embedding the link. Through further optimization of the device structure to eliminate parasitic capacitance and reduce resistance, we expect to achieve even lower driving voltage of 0.5 V_{pp}, resulting in a low energy consumption of 13.6 fJ/bit with a high E-O bandwidth of 52 GHz. Such a MOSCAP Si-MRM driven by a high mobility TCO gate would exhibit the potential for high-speed E-O modulation with sub-volt driving voltages, thereby paving the way for future advancements in energy-efficient optical communication and computation systems.

Results

Device Design

Fig. 1 illustrates the design of the ITiO-gated MOSCAP Si-MRM, including a 3D schematic diagram and a cross-sectional view of the active region. The device comprises a 300 nm thick Si rib waveguide with a 100 nm slab thickness. A waveguide width of 300 nm is selected to enhance the E-O efficiency, while a radius of 8 μm is chosen to reduce the bending loss (Supplementary Information II). The Si doping profile of p (1×10^{17} cm^{-3}), p+ (3×10^{18} cm^{-3}), and p++ (1×10^{20} cm^{-3}) are designed to reduce the series resistance without compromising the optical absorption in the Si waveguide. The entire device has a background Si p-doping, and the p+ region covers the top of the ring waveguide and part of the Si slab. The p++ region is placed 600 nm away from the ring waveguide to maintain the Q-factor. Such a doping design allows the passive Si microring resonator to achieve a high Q-factor of 20,000 near the critical coupling condition. The active E-O modulation region, which represents approximately 62.5% of the microring circumference (L = 31.4 μm), consists of a 10 nm thick HfO_2 insulator layer and a 14 nm ITiO layer on the top. The Ni/Au electrodes traverse the bus waveguide via the top SiO_2 waveguide cladding, forming ohmic contacts with the ITiO gate and the Si substrate of the MOSCAP.

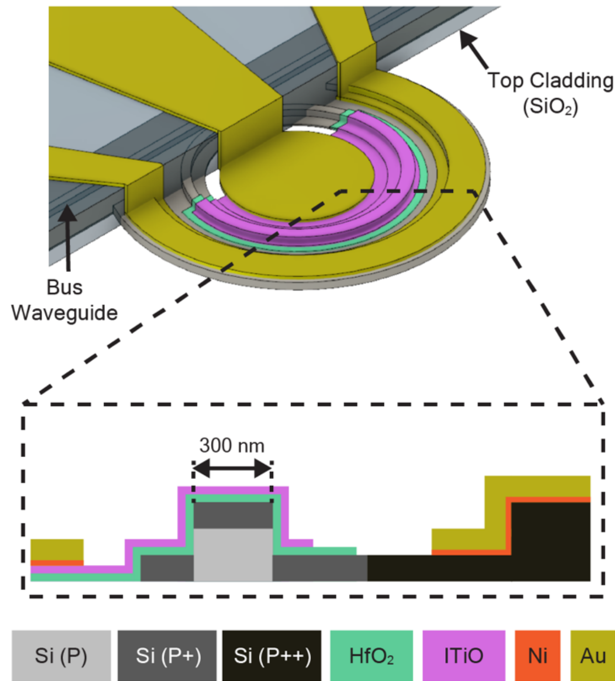

Fig. 1: 3D schematic diagram of an ITiO-gated MOSCAP Si-MRM. The dashed line box shows the cross-sectional view in the active region of the ITiO-gated MOSCAP Si-MRM.

Fig. 2(a) shows the simulated carrier density distribution in the cross-sectional waveguide of the ITiO-gated MOSCAP Si-MRM in the active region. When a negative bias is applied, holes and electrons accumulate at the Si/HfO_2 and HfO_2/ITiO interfaces, respectively. Accumulated electrons within the ITiO layer is less than 1nm thick, which is significantly thinner than the hole accumulation layer in the Si waveguide due to the different Debye lengths caused by the varying carrier concentration and dielectric constant[37]. Fig. 2(b) presents the optical mode profile of the transverse-electric (TE) mode in the ITiO-gated MOSCAP Si-MRM. Due to the bending ring waveguide, the optical mode profile shifts toward the outer sidewall of the waveguide. Upon a negative bias, the optical mode interacts with the accumulation charges in both ITiO and Si, enabling E-O modulation and blue-shifting the resonant wavelength ($\Delta\lambda_{res}$). Our previous studies have discussed that phase modulation with moderate index change is majorly determined by the total charge variation, allowing us to simplify the simulation model to a uniform distribution with 1 nm thick accumulation layers, aligning well with experimental results[38,39]. Therefore, Fig. 2(b) also provides a zoomed-in view of the optical mode profile at the HfO_2/ITiO interfaces, showcasing examples at 0 V and -1 V biases with a 1 nm thick uniform accumulation layer. Fig. 2(c) shows the simulated transmission spectra under different gate biases. Our simulation assumes a dielectric constant of 12 for HfO_2 and carrier mobility of 62 $cm^2/(V \cdot s)$ with a concentration of 1.2×10^{20} cm^{-3} for ITiO, chosen to align with

the experimental material properties (Supplementary Information III, IV). Using such parameters, the ITiO-gated MOSCAP Si-MRM achieves a high Q-factor of 5000 at 0V with an E-O efficiency of 125 pm/V in the accumulation mode. The simulation results also demonstrate that the ITiO-gated MOSCAP Si-MRM can achieve a 7.6 dB extinction ratio (ER) with 3 dB insertion loss (IL) using only 0.8 V_{pp}, highlighting the potential for efficient modulation.

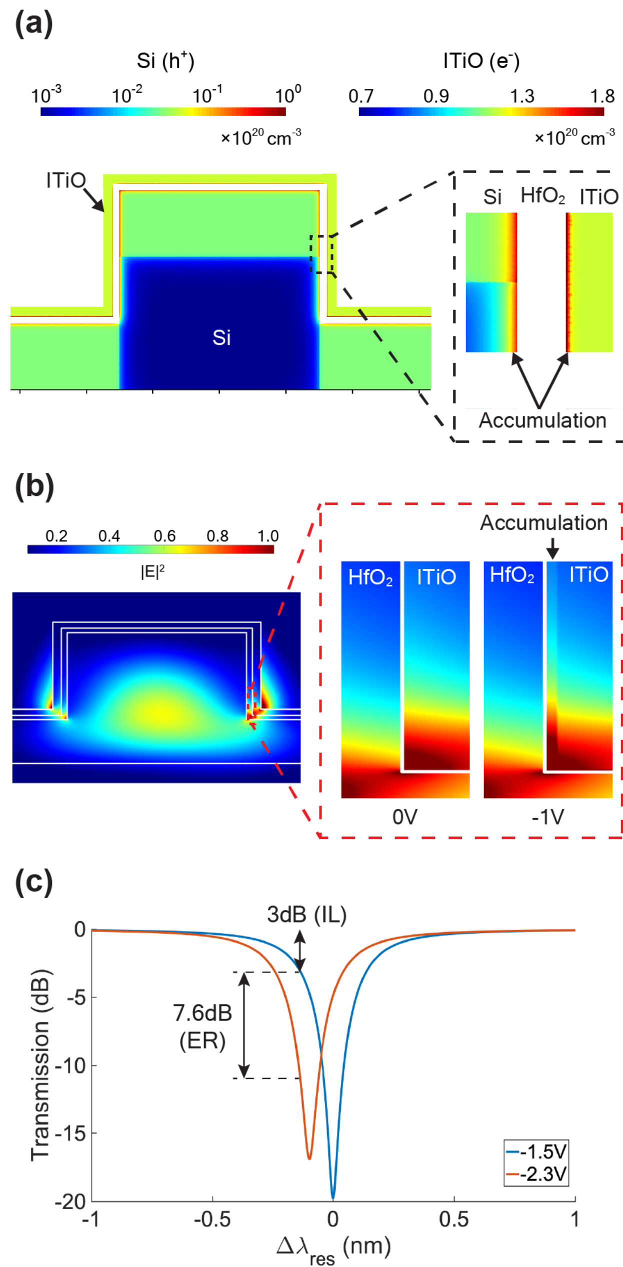

Fig. 2: (a) Simulated carrier distribution in the cross-sectional waveguide of the ITiO-gated MOSCAP Si-MRM at a bias of -2.3 V. Negative bias on ITiO gate results in hole accumulation at the Si/HfO_2 interface and electron accumulation at the HfO_2/ITiO interface. Note: the color bars representing carrier concentrations for Si and ITiO

are in different scales. (b) Optical mode profile of the TE mode in the ITiO-gated MOSCAP Si-MRM waveguide. Zoomed-in views at the HfO_2/ITiO interfaces at 0 V and -1 V biases. (c) Static simulation of the blue-shifted spectra under -1.5 V and -2.3 V.

Fig. 3(a) presents the scanning electron microscope (SEM) image of the passive Si microring resonator, which was fabricated by Intel's 300-millimeter silicon-on-insulator (SOI) photonics process. To complete the entire process of the active ITiO-gated MOSCAP Si-MRM, we continued the fabrication using the cleanroom facility at Oregon State University. The SiO_2 top cladding in the active region was then etched by reactive ion etching (RIE). Despite the high etching selectivity between SiO_2 and Si, some Si waveguide was still inadvertently etched during the process. As a result, the width of the Si microring waveguide was slightly narrower than the designed value, measuring at 290 nm, as depicted in Fig. 3(b). After the entire fabrication process, Fig. 3(c) shows a top view of the fabricated ITiO-gated MOSCAP Si-MRM. Additionally, Fig. 3(d) provides a zoomed-in SEM image highlighting the ITiO region, represented by a false purple color.

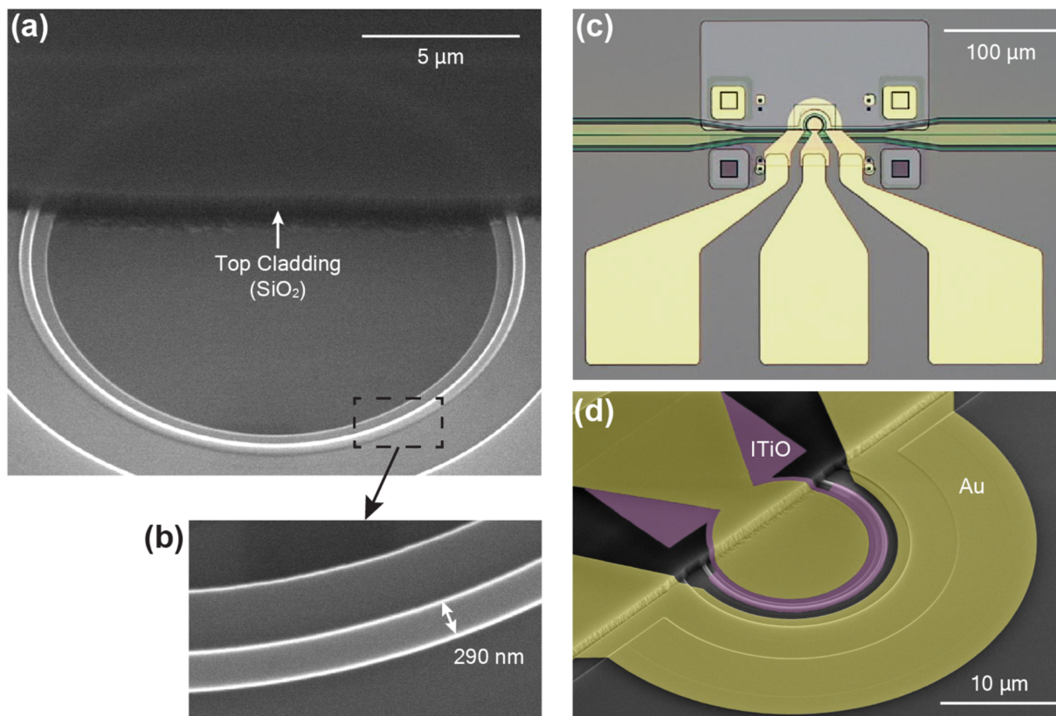

Fig. 3: (a) SEM image of the passive Si microring resonator fabricated by Intel's photonics fab, showing the etched SiO_2 top cladding in the active region after RIE. (b) Top-view SEM image highlighting the narrow Si microring waveguide. (c) Optical image of the fabricated ITiO-gated MOSCAP Si-MRM with high-speed Ni/Au electrodes. (d) SEM image of the fabricated ITiO-gated MOSCAP Si-MRM with false colors.

DC Characterization

The ITiO-gated MOSCAP Si-MRM was designed to operate at O-band. The normalized transmission spectra with various gate voltages are shown in Fig. 4(a). The device was designed near critical coupling, resulting in a deep resonant dip to enable a modulation condition with an ER exceeding 6 dB and an IL of 3 dB. Applying a negative bias to the ITiO gate causes the accumulated carriers in both the Si waveguide and ITiO gate, resulting in $\Delta\lambda_{res}$. Simultaneously, such accumulated charges also increase optical absorption and decrease the Q-factor. The measured Q-factors and $\Delta\lambda_{res}$ are plotted in Fig. 4(b). The ITiO-gated MOSCAP Si-MRM exhibits a Q-factor of approximately 4600 at 0 V, supporting an optical bandwidth of 50 GHz. For gate biases ranging from 0 V to -1.5 V, the ITiO-gated MOSCAP Si-MRM operates in the depletion mode due to the non-ideal flat-band voltage (V_{FB}), achieving an E-O efficiency of 87 pm/V. Once the negative bias exceeds -1.5 V, the MOSCAP transitions into the accumulation mode, and $\Delta\lambda_{res}$ becomes more linear, leading to a higher E-O efficiency of 117 pm/V, corresponding to a very low V_{π}•L of 0.12 V•cm. Therefore, the ITiO-gated MOSCAP Si-MRM operates in the accumulation mode to achieve a low driving voltage (V_{pp}). Additionally, it is worth noting that the experimental Q-factor (4600) and E-O efficiency (117 pm/V) obtained were only slightly lower than the simulated values of Q-factor (5000) and E-O efficiency (125 pm/V) with acceptable error margin of 8%. The modulation wavelength (λ_{MOD}) was fine-tuned by a tunable laser to ensure an IL of 3 dB at -1.5 V. The optical transmission for different gate biases at λ_{MOD} is shown in Fig. 4(c). An ER of 6 dB and an IL of 3 dB can be achieved with a bias voltage of -1.9 V and a voltage swing of 0.8 V_{pp} (-1.5 V ~ -2.3 V). The observed ER, though slightly lower than the expected value, can be attributed to the slightly lower experimental Q-factor and E-O efficiency.

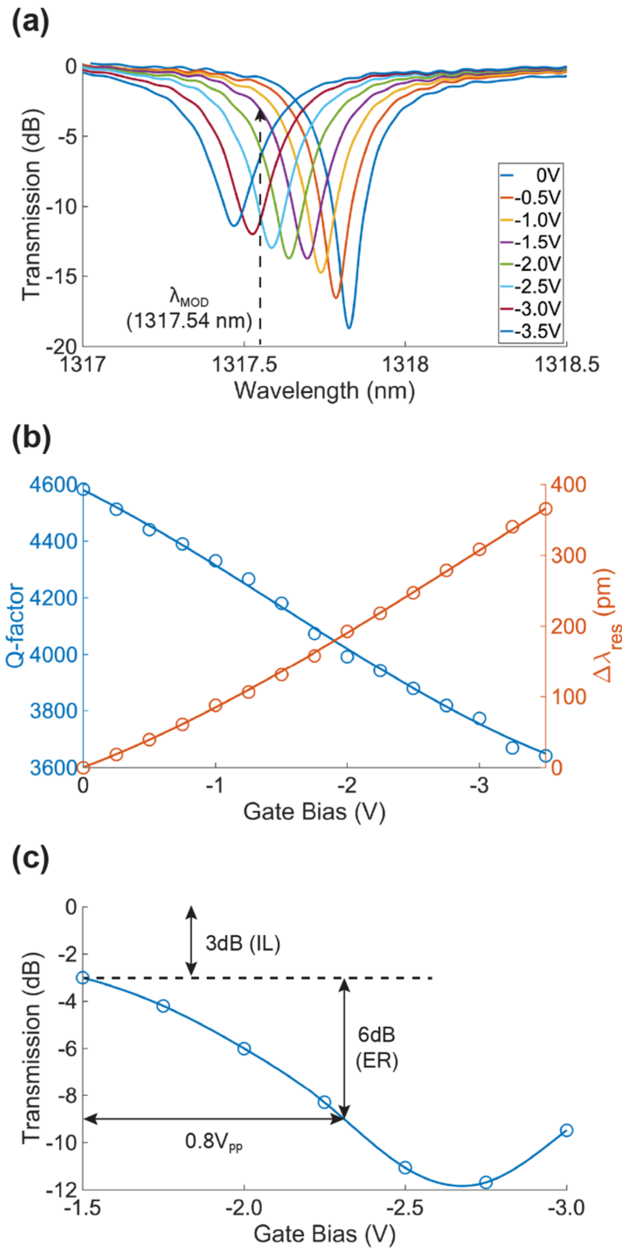

Fig 4. (a) Normalized transmission spectra of the ITiO-gated MOSCAP Si-MRM with different gate biases. (b) Measured Q-factor (blue) and $\Delta\lambda_{res}$ (orange) as a function of the gate bias. (c) Transmission at λ_{MOD} (1317.54 nm) with respect to the gate voltage. It biases at -1.9 V with 0.8 V_{pp} (-1.5 V to -2.3 V) to achieve an ER of 6 dB with an IL of 3 dB.

High-Speed Characterization

The E-O response (S_{21}) of the ITiO-gated MOSCAP Si-MRM was measured under the condition of 3 dB IL at -1.5 V. By varying the frequency of the input sine wave driving signal, the corresponding output RF power was measured by a microwave spectrum analyzer (MSA). Fig. 5(a) shows an example of the output signal on the

MSA at 10 GHz. Since the output signals were amplified by a 42 GHz photodetector with a built-in transimpedance amplifier, the output RF power was normalized to the RF power at a low frequency of 500 MHz. The measured and normalized data were plotted in Fig. 5(b), with the fitting curve represented by an orange dashed line. The E-O response exhibits the peaking effect[40], enhancing the 3 dB bandwidth to 11 GHz. It provides the potential for supporting the ITiO-gated MOSCAP Si-MRM in achieving non-return-to-zero (NRZ) modulation at data rates exceeding 20 Gb/s.

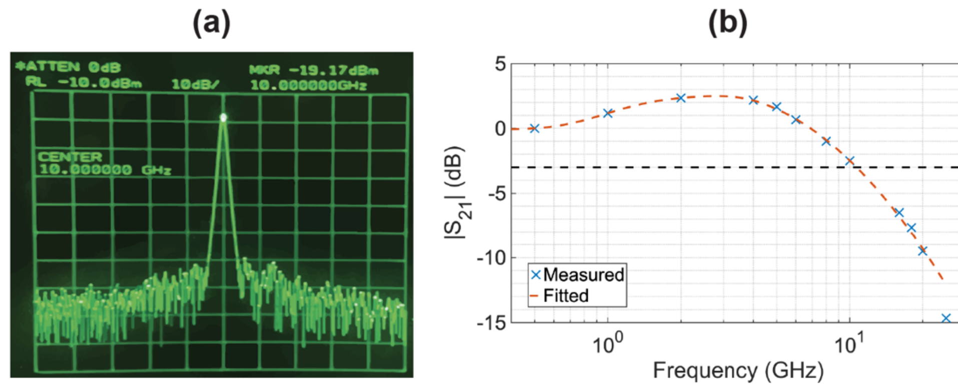

Fig. 5: (a) Output signal on the MSA at 10 GHz. (b) Normalized E-O response (S_{21}) of the ITiO-gated MOSCAP Si-MRM in the frequency range of 500 MHz to 25 GHz. Note: A tunable laser was fine-tuned to the input wavelength to achieve an IL of 3 dB at -1.5 V.

For the E-O modulation measurement, the ITiO-gated MOSCAP Si-MRM was biased at the IL of 3 dB at -1.5 V and driven by 0.8 V_{pp} NRZ pseudorandom binary sequence (PRBS) signals. PRBS9 was used for data rates lower than 10Gb/s, and PRBS15 was employed for higher data rates. Since the capacitance changes with the applied gate bias as indicated in the C-V characteristics (Supplementary Information IV), the capacitance (after eliminating the parasitic capacitance) was found to be 333 fF at -1.9 V, which corresponds to the center of the 0.8 V voltage swing (-1.5 V to -2.3 V). Considering the modulation energy consumption ($CV^2/4$), the estimated energy consumption is 53 fJ/bit. Fig. 6(a) presents the obtained optical eye diagrams at different data rates using a digital communication analyzer (DCA). It is evident from the diagrams that the eye remains open even at the data rate of 25 Gb/s. To push for even higher data rates, the S_{21} data from Fig. 5(b) was utilized as the input into the arbitrary waveform generator (AWG) to pre-emphasize the signals to enhance the quality of received signals at the DCA. Additionally, the ITiO-gated MOSCAP Si-MRM was driven with a higher voltage. Fig. 6(b) shows the optical eye diagrams obtained through this approach, incorporating the pre-emphasis signals and a driving voltage of 1.75 V_{pp}. Compared to Fig. 6(a), it becomes apparent that the open eye at 25 Gb/s is even clearer,

and the eyes are successfully opened up to 35 Gb/s.

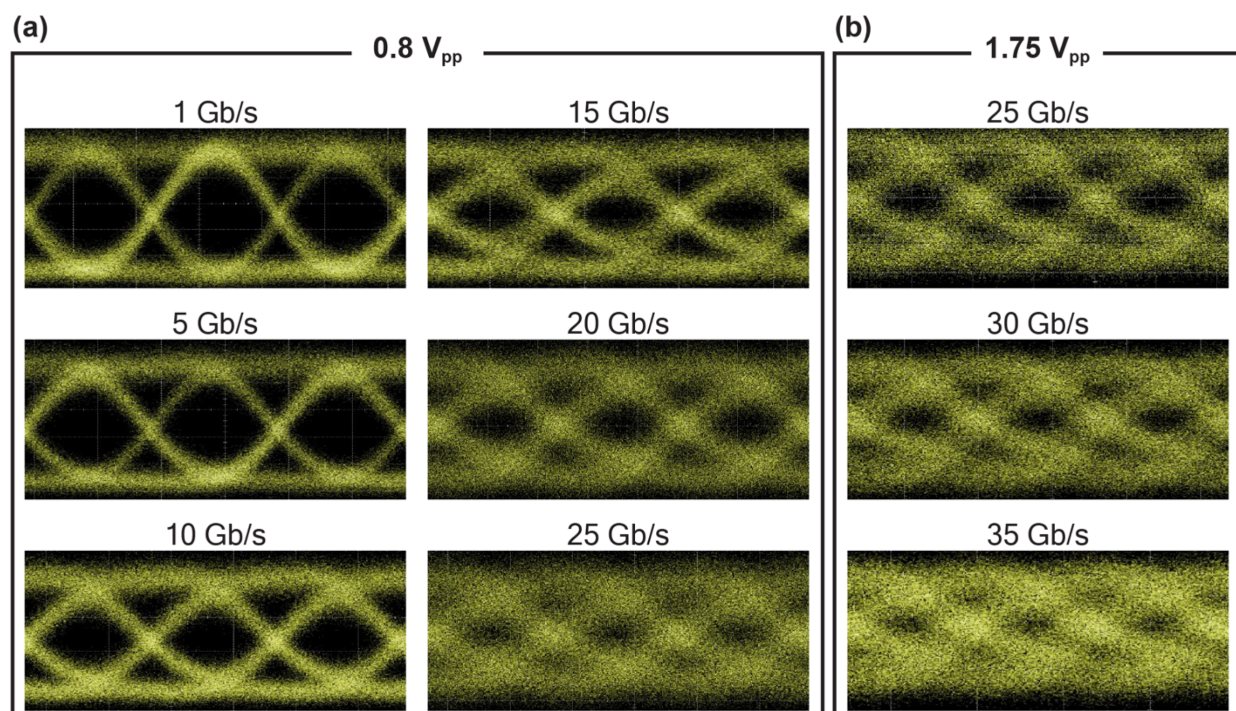

Fig. 6: Measured NRZ modulation eye diagrams of the ITiO-gated MOSCAP Si-MRM with different data rates. (a) driving voltage of 0.8 V_{pp} without any pre-emphasis signal. (b) driving voltage of 1.75 V_{pp} with the pre-emphasis signal.

Device Optimization

Fig. 5(b) demonstrated that the ITiO-gated MOSCAP Si-MRM achieved an E-O bandwidth of 11 GHz, which is limited by the RC bandwidth since the photon lifetime-limited bandwidth supports up to 50 GHz with a Q-factor of 4600. The device's high overall capacitance of 500 fF (Supplementary Information IV) hinders the bandwidth improvement. Although higher doping concentration of the TCO and Si materials can lower the resistance, it will introduce greater optical absorption loss that can suppress the Q-factor with the price of higher driving voltages. To maintain the E-O efficiency, it is necessary to reduce the overall capacitance. In the current device, the MOSCAP is formed by covering the top and two sidewalls of the waveguide with ITiO, as well as the 500 nm width of the Si slab. By calculation, the outer sidewall of the ring contributes over 50% of the total modulation, while the top of the waveguide and the slab act more like parasitic capacitance with minimal contribution to E-O modulation (Supplementary Information V). This insight analysis suggests that the total capacitance can be significantly reduced by covering only the outer sidewall of the ring, as illustrated in Fig. 7(a). In parallel, the thickness of HfO_2 is reduced from 10 nm to 6 nm, enhancing the capacitance density and improving E-O efficiency. Furthermore, employing a higher mobility TCO, such as hydrogen-doped indium oxide (IHO)[41], not

only improves the Q-factor by reducing the optical loss but also decreases the series resistance. IHO has reported a high mobility of 150 $cm^2/(V{\cdot}s)$ with a concentration of 1.5×10^{20} cm^{-3}. Assuming the active E-O modulation region occupies 70% of the microring, this structure allows the modulator to achieve a Q-factor of 6000 at 0V. When the device is biased at -1.5 V, the Q-factor slightly reduces to 5600 with an E-O efficiency of 148 pm/V, as depicted in Fig. 7(b). Hence it can achieve a 6 dB ER with a 3 dB IL using only 0.5 V_{pp}. Moreover, with this improved structure and the material properties, the total capacitance can be reduced from 500 fF to 218 fF, and the total series resistance will be 18 Ω, effectively supporting an RC bandwidth up to 40.6 GHz. The simulated E-O bandwidth extends to 52 GHz, as shown in Fig. 7(c). In addition, the energy efficiency can be improved to 13.6 fJ/bit.

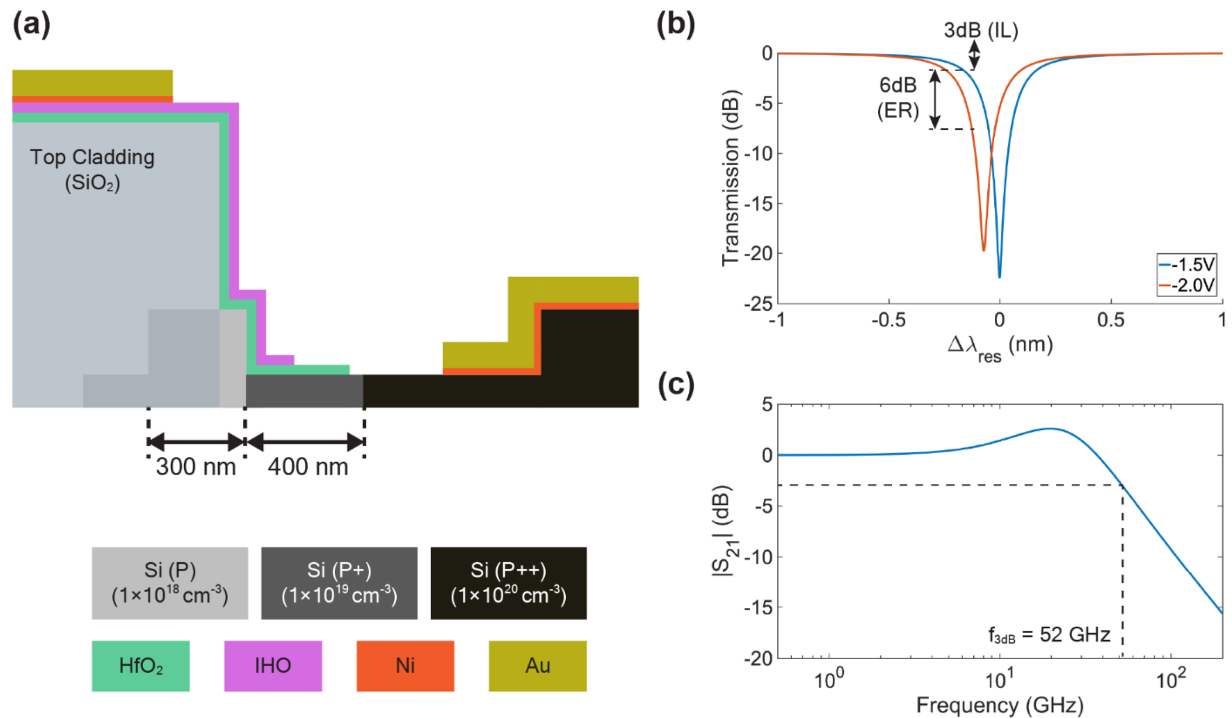

Fig. 7: (a) The cross-sectional view in the active region of the MRM with TCO only covering the outer sidewall of the ring. (b) Static simulation of the shifted spectra under -1.5 V and -2.0 V. (c) Simulated E-O response (S_{21}) of the MRM with 52 GHz bandwidth.

Discussion

This work successfully demonstrated the integration between silicon photonics and high-mobility TCO material to create a highly efficient ITiO-gated MOSCAP Si-MRM. The device was co-fabricated by Intel's photonics fab and TCO patterning processes at Oregon State University. It exhibited an exceptional E-O efficiency of 117 pm/V,

along with a V_{π}•L of 0.12 V•cm. With an E-O bandwidth of 11 GHz, it achieved a 25 Gb/s open eye at a sub-volt V_{pp} of 0.8 V with an energy efficiency of 53 fJ/bit. With further optimization of the device structure, it has the potential to achieve a 0.5 V_{pp} while increasing the E-O bandwidth to 52 GHz, enabling data encoding at 100 Gb/s for the next generation of high-speed optical communication with an energy efficiency of 13.6 fJ/bit. In conclusion, the highly efficient ITiO-gated MOSCAP Si-MRM presented in this work has a significant impact on energy-efficient optical communication and computation. Its sub-volt driving voltage offers the feasibility of direct CMOS driving without any voltage amplifier, which can potentially reduce the transmitter side power consumption by an order of magnitude. It will also bridge the gap of the driving voltage between neuromorphic computing and photonic modulators, enabling low-energy photonic computing for artificial intelligence.

Methods

Fabrication

The passive Si microring resonator was fabricated on a SOI wafer using Intel's photonics fab. The Si microring has a narrow waveguide width of 300 nm and a waveguide height of 300 nm while leaving a 100 nm thick Si slab to ensure good optical mode confinement in the Si waveguide and proper electrical conduction. To create the MOSCAP on the microring, the top SiO_2 cladding in the active region of the microring was selectively patterned using regular photolithography, followed by RIE, as shown in Fig. 3(a). Next, a 10 nm HfO_2 insulator layer was deposited on the entire SOI substrate by atomic layer deposition (ALD) using tertrakis (eythylmetylamido)-Hf (TEMA) and H_2O at 300ºC. Subsequently, a 14 nm layer ITiO was RF-sputtered onto the HfO_2 layer at a high substrate heating temperature of 500°C, which covered the entire wafer with ITiO. The ITiO layer in the active region was patterned using a two-step process. Electron beam lithography (EBL) with RIE was employed to accurately define the desired ITiO pattern within the active region. Subsequently, regular photolithography with wet etching (ITO etchant) was used to remove any residual ITiO. After these two steps, the ITiO layer only covered approximately 62.5% of the microring circumference. Prior to the metal deposition, the HfO_2 layer in the Si contact region was patterned using EBL and removed by RIE. The Ni/Au electrical contacts were patterned on the ITiO gate and the Si substrate using EBL, followed by thermal evaporation and lift-off. These contacts were patterned approximately 1.2 µm away from the microring waveguide. Finally, the Ni/Au coplanar ground-signal-ground (GSG) electrode pads were patterned using regular photolithography followed by thermal evaporation and lift-off and were connected to the electrical contacts patterned in the previous step.

Eye Diagrams Testing

Fig. 8(a) illustrates the testing setup utilized for measuring optical eye diagrams. A PRBS electrical signal was generated using a 92 GSa/s AWG (Keysight M8196A), and it was combined with a DC bias through a 50-GHz bias tee (Keysight 11612B), ensuring optimal modulation of the electrical signal. Subsequently, this combined signal was applied to the device via an Infinity 40-GHz high-speed GSG probe. Simultaneously, a tunable laser (TL) (Santec TSL-570) was employed to generate the optical input, and the optical signals were coupled in and out through waveguide grating couplers. The modulated optical signal was then amplified by an O-Band Praseodymium-Doped Fiber Amplifier (PDFA) (Thorlabs PDFA100) before being detected by a 65 GHz optical module (Keysight N1030A) plugged to a DCA (Keysight N1000A). Finally, the DCA enables the acquisition of the optical eye diagram.

E-O Response Testing

The E-O response shown in Fig. 5(b) was characterized using the experimental setup depicted in Fig. 8(b). The single-frequency sine wave generated by the AWG was combined with a DC voltage using the bias tee before being utilized to drive the ITiO-gated MOSCAP Si-MRM. The device was modulated by the input single-frequency sine wave, resulting in an output-modulated optical signal detected by a 42 GHz photodetector with a built-in transimpedance amplifier (Thorlabs RXM42AF). Subsequently, the detected signal was further analyzed using a 26 GHz MSA (HP8562A). To examine the frequency-dependent behavior of the E-O response, the input frequency of the sine wave was scanned, and the corresponding changes in the output power displayed on the MSA were observed. By systematically measuring the output power at different input frequencies, the S_{21} response of the ITiO-gated MOSCAP Si-MRM was characterized.

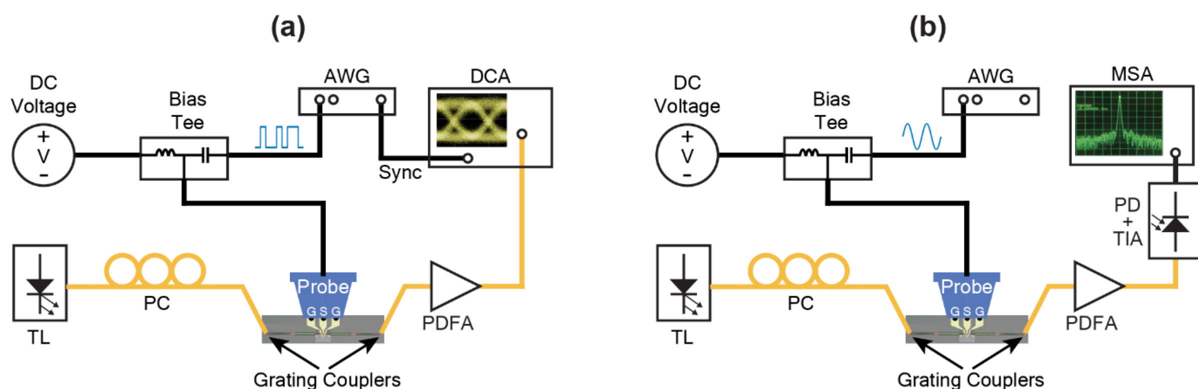

Fig. 8: Schematic of high-speed testing setups for (a) eye diagrams, (b) E-O response.

References

1. Xu, Q., Schmidt, B., Pradhan, S. & Lipson, M. Micrometre-scale silicon electro-optic modulator. *Nature* **435**, 325–327 (2005).
2. Bogaerts, W. *et al.* Silicon microring resonators. *Laser Photonics Rev.* **6**, 47–73 (2012).
3. Xu, Q., Fattal, D. & Beausoleil, R. G. Silicon microring resonators with 1.5-μm radius. *Opt. Express* **16**, 4309–4315 (2008).
4. Dong, P. Silicon Photonic Integrated Circuits for Wavelength-Division Multiplexing Applications. *IEEE J. Sel. Top. Quantum Electron.* **22**, 370–378 (2016).
5. Guarino, A., Poberaj, G., Rezzonico, D., Degl'Innocenti, R. & Günter, P. Electro–optically tunable microring resonators in lithium niobate. *Nat. Photonics* **1**, 407–410 (2007).
6. Lu, X., Moille, G., Rao, A., Westly, D. A. & Srinivasan, K. Efficient photoinduced second-harmonic generation in silicon nitride photonics. *Nat. Photonics* **15**, 131–136 (2021).
7. Eppenberger, M. *et al.* Resonant plasmonic micro-racetrack modulators with high bandwidth and high temperature tolerance. *Nat. Photonics* **17**, 360–367 (2023).
8. Fathololoumi, S. *et al.* 1.6 Tbps Silicon Photonics Integrated Circuit and 800 Gbps Photonic Engine for Switch Co-Packaging Demonstration. *J. Light. Technol.* **39**, 1155–1161 (2021).
9. Chan, D. W. U., Wu, X., Lu, C., Lau, A. P. T. & Tsang, H. K. Efficient 330-Gb/s PAM-8 modulation using silicon microring modulators. *Opt. Lett.* **48**, 1036–1039 (2023).
10. Zhang, Y. *et al.* 240 Gb/s optical transmission based on an ultrafast silicon microring modulator. *Photonics Res.* **10**, 1127–1133 (2022).
11. Margalit, N. *et al.* Perspective on the future of silicon photonics and electronics. *Appl. Phys. Lett.* **118**, 220501 (2021).
12. Siew, S. Y. *et al.* Review of Silicon Photonics Technology and Platform Development. *J. Light. Technol.* **39**, 4374–4389 (2021).
13. Chan, D. W. U. *et al.* Ultra-Wide Free-Spectral-Range Silicon Microring Modulator for High Capacity WDM. *J. Light. Technol.* **40**, 7848–7855 (2022).
14. Yuan, Y. *et al.* A 100 Gb/s PAM4 Two-Segment Silicon Microring Resonator Modulator Using a Standard Foundry Process. *ACS Photonics* **9**, 1165–1171 (2022).
15. Pandey, A., Dwivedi, S., Zhenzhou, T., Pan, S. & Van Thourhout, D. Nonreciprocal Light Propagation in a Cascaded All-Silicon Microring Modulator. *ACS Photonics* **8**, 1997–2006 (2021).
16. Liu, J. *et al.* Ultrahigh extinction ratio silicon micro-ring modulator by MDM resonance for high speed PAM-4 and PAM-8 signaling. *Opt. Express* **30**, 25672–25684 (2022).
17. Streshinsky, M. *et al.* Low power 50 Gb/s silicon traveling wave Mach-Zehnder modulator near 1300 nm. *Opt. Express* **21**, 30350–30357 (2013).
18. Yong, Z. *et al.* U-shaped PN junctions for efficient silicon Mach-Zehnder and microring modulators in the O-band. *Opt. Express* **25**, 8425–8439 (2017).
19. Sicard, E. & Trojman, L. Introducing 5-nm FinFET technology in Microwind. URL: https://hal.science/hal-03254444 (2021).
20. Li, H. *et al.* A 106 Gb/s 2.5 Vppd Linear Microring Modulator Driver with Integrated Photocurrent Sensor in 28nm CMOS. in *OFC* M2D.1 (2022).
21. Liu, A. *et al.* A high-speed silicon optical modulator based on a metal-oxide-semiconductor capacitor. *Nature* **427**, 615–618 (2004).
22. Hiraki, T. *et al.* Heterogeneously integrated III-V/Si MOS capacitor Mach-Zehnder modulator. *Nat. Photonics* **11**, 482–485 (2017).
23. Cheung, S. *et al.* Demonstration of a 17 × 25 Gb/s Heterogeneous III-V/Si DWDM Transmitter Based on (De-) Interleaved Quantum Dot Optical Frequency Combs. *J. Light. Technol.* **40**, 6435–6443 (2022).
24. Thiessen, T. *et al.* 30 GHz heterogeneously integrated capacitive InP-on-Si Mach-Zehnder modulators. *Opt. Express* **27**, 102–109 (2019).
25. Sorianello, V. *et al.* Graphene–silicon phase modulators with gigahertz bandwidth. *Nat. Photonics*

12, 40–44 (2018).

26. Wood, M. G. *et al.* Gigahertz speed operation of epsilon-near-zero silicon photonic modulators. *Optica* **5**, 233–236 (2018).
27. Li, E., Gao, Q., Chen, R. T. & Wang, A. X. Ultracompact Silicon-Conductive Oxide Nanocavity Modulator with 0.02 Lambda-Cubic Active Volume. *Nano Lett.* **18**, 1075–1081 (2018).
28. Ma, Z., Li, Z., Liu, K., Ye, C. & Sorger, V. J. Indium-Tin-Oxide for High-performance Electro-optic Modulation. *Nanophotonics* **4**, 198–213 (2015).
29. Sakib, M. *et al.* A high-speed micro-ring modulator for next generation energy-efficient optical networks beyond 100 Gbaud. in *CLEO* SF1C.3 (2021).
30. Campenhout, J. Van *et al.* Low-voltage, low-loss, multi-Gb/s silicon micro-ring modulator based on a MOS capacitor. in *OFC* OM2E.4 (2012).
31. Zhang, W. *et al.* Harnessing plasma absorption in silicon MOS ring modulators. *Nat. Photonics* **17**, 273–279 (2023).
32. Liang, D. *et al.* An Energy-Efficient and Bandwidth-Scalable DWDM Heterogeneous Silicon Photonics Integration Platform. *IEEE J. Sel. Top. Quantum Electron.* **28**, 1–19 (2022).
33. Kong, D., Liu, Y., Ding, Y., Hu, H. & Luan, C. *Ultrahigh-modulation-efficiency graphene-silicon micro-ring modulator*. DOI:10.21203/rs.3.rs-2921645/v1 (2023).
34. Hsu, W.-C., Nujhat, N., Kupp, B., Conley, J. F. & Wang, A. X. On-chip wavelength division multiplexing filters using extremely efficient gate-driven silicon microring resonator array. *Sci. Rep.* **13**, 5269 (2023).
35. Zhou, B., Li, E., Bo, Y. & Wang, A. X. High-Speed Plasmonic-Silicon Modulator Driven by Epsilon-Near-zero Conductive Oxide. *J. Light. Technol.* **38**, 3338–3345 (2020).
36. Li, E., Zhou, B., Bo, Y. & Wang, A. X. High-Speed Femto-Joule per Bit Silicon-Conductive Oxide Nanocavity Modulator. *J. Light. Technol.* **39**, 178–185 (2021).
37. Hsu, W.-C., Zhou, B. & Wang, A. X. MOS Capacitor-Driven Silicon Modulators: A Mini Review and Comparative Analysis of Modulation Efficiency and Optical Loss. *IEEE J. Sel. Top. Quantum Electron.* **28**, 1–11 (2022).
38. Li, E. & Wang, A. X. Theoretical Analysis of Energy Efficiency and Bandwidth Limit of Silicon Photonic Modulators. *J. Light. Technol.* **37**, 5801–5813 (2019).
39. Hsu, W.-C., Li, E., Zhou, B. & Wang, A. X. Characterization of field-effect mobility at optical frequency by microring resonators. *Photonics Res.* **9**, 615–621 (2021).
40. Müller, J. *et al.* Optical Peaking Enhancement in High-Speed Ring Modulators. *Sci. Rep.* **4**, 6310 (2014).
41. Koida, T., Ueno, Y. & Shibata, H. In2O3-Based Transparent Conducting Oxide Films with High Electron Mobility Fabricated at Low Process Temperatures. *Phys. status solidi* **215**, 1700506 (2018).

Acknowledgements

This work is supported by the Intel URC project 76084461, the NSF GOALI project 2240352, the AFOSR MURI project FA9550-17-1-0071, and the NASA ESI program 80NSSC23K0195. Besides, we would like to thank the Materials Synthesis and Characterization Facility (MaSC) and the Electron Microscopy Facility at Oregon State University for our device fabrication. MaSC is part of the Northwest Nanotechnology Infrastructure, a National Nanotechnology Coordinated Infrastructure site at Oregon State University supported in part by the National Science Foundation (grant NNCI-1542101). The authors acknowledge Meer Sakib for the helpful discussion in

design and characterization, Duanni Huang and James Jaussi for technical discussions.

Author contributions statement

W.H. and A.X.W. were involved in the design, experiments, and manuscript writing. N.N. was involved in device fabrication. B.K. and J.F.C. were involved in atomic layer deposition. H.R. and R.K. were involved in the design. All authors reviewed the manuscript.

Additional information

Disclosures: The authors declare no conflicts of interest.

Data availability: All data generated or analyzed during this study are included in this published article and its supplementary information files.

Sub-Volt High-Speed Silicon MOSCAP Microring Modulator Driven by High Mobility Conductive Oxide (Supplementary Information)

Wei-Che Hsu[1,2], Nabila Nujhat[1], Benjamin Kupp[1], John F. Conley, Jr[1], Haisheng Rong[3], Ranjeet Kumar[3], and Alan X. Wang[1,2,*]

[1]School of Electrical Engineering and Computer Science, Oregon State University, Corvallis, Oregon 97331, USA

[2]Department of Electrical and Computer Engineering, Baylor University, One Bear Place #97356, Waco, Texas 76798, USA

[3]Intel Corporation, 3600 Juliette Ln, Santa Clara, CA 95054

[*]alan_wang@baylor.edu

I. Review of High-Speed Si Microring Modulators Driven by Various Structures

Table 1 summarizes published state-of-the-art Si microring modulators (Si-MRM). Typically, the Q-factor of Si-MRM is designed below 5000 to achieve an optical bandwidth above 40 GHz. Most Si-MRMs require a high driving voltage (V_{pp}) for electro-optic (E-O) modulation due to their low E-O efficiency. Higher insertion loss results in a sharper resonance. Therefore, some existing Si-MRMs sacrifice the insertion loss to lower the driving voltage. Integrating the plasmonic/E-O polymer phase shifter into the Si-MRM achieved exceptionally high E-O efficiency. However, the plasmonic structure is inherently lossy and reduces the Q-factor of the Si-MRM. Our work on titanium-doped indium oxide (ITiO)-gated MOSCAP Si-MRM not only offers enhanced E-O-efficiency but also maintains a sufficient Q-factor to achieve a low driving voltage and support a large optical bandwidth.

Table 1: Comparison of performance of the high-speed MRM.

Modulator structure	Operation band	Q-factor	E-O efficiency (pm/V)	V_{pp} (V)	$V_{\pi}L$ (V•cm)	Energy efficiency (fJ/bit)	IL (dB)	f_{3dB} (GHz)	Data rate (Gb/s)	Ref.
Reversed PN junction	O	4200	~40	0.8 (~2)	0.53	5.3	9 (~3)	58	128	[1]
Reversed PN junction	O	4500	26.4	3	0.825	~85.5	3	>60	120	[2]
MOSCAP-Si	C	3500	130	1.5	0.24	180	3	1.7	3	[3]

MOSCAP-Si	C	4600	40	1.6	0.7	~24.32	9	50	112	4
MOSCAP-III-V	O	8143	~20	4	1	~250	2	15	28	5
MOSCAP-graphene	C	3396	~33	6	-	21	5.8	52	40	6
Plasmonic-Polymer	C	700	178	4	0.015	12.3	4	176	220	7
MOSCAP-ITiO	O	4600	117	0.8	0.12	53	3	11	25	This work

~ Didn't mention it in the article. Measured from spectra or calculated based on other parameters in the articles.
- Not available in the article

II. Optimizing Radius for ITiO-Gated MOSCAP Si-MRM

The ITiO-gated MOSCAP Si-MRM is designed to achieve a Q-factor ranging from 5000 to 6000 that ensures sufficient optical bandwidth while minimizing the driving voltage. Once the ITiO is deposited on the Si ring waveguide, it introduces optical absorption losses that can decrease the Q-factor. To maintain the Q-factor after ITiO deposition, it is crucial to ensure that the loss from the Si ring waveguide is negligible compared to the optical absorption from ITiO. In other words, the Q-factor of the passive Si microring resonator should be significantly higher than 5000, for instance, around 20000. To determine the appropriate radius for the design, Fig. S1 presents the simulated loss of the bent passive Si waveguide at various radii. The geometry and doping profiles of the Si waveguide remain consistent with the design illustrated in Fig. 1. Since the waveguide is designed to be 300 nm wide, it exhibits significant bending losses at small radii. As the radius increases, the loss decreases accordingly. It is observed that when the radius exceeds 8 μm, the loss of the passive Si microring becomes sufficiently low to support a Q-factor greater than 20000. Based on the simulation results, the radius of 8 μm is chosen for the ITiO-gated MOSCAP Si-MRM design. It ensures that the passive Si microring resonator maintains a high Q-factor, even after the deposition of ITiO, enabling the desired performance.

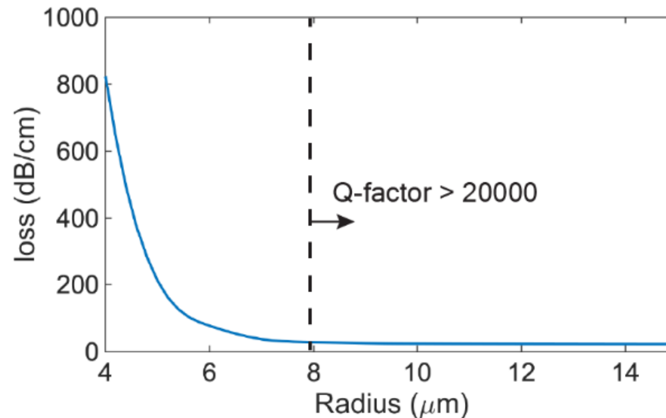

Fig. S1: Simulated optical loss of bent Si waveguide at various radii.

III. ITiO Thin Film Characterization

The ITiO material was characterized by RF-sputtering it onto lime glass in the same batch as the device. The sputtering process maintained consistent conditions, including a high substrate heating temperature of 500 °C. The thickness of the ITiO layer was determined by an ellipsometer (Film Sense FS-1). To evaluate the mobility and carrier concentration of the ITiO material, Hall measurements were performed using a Lake Shore M91 FastHall system. Furthermore, to obtain the carrier concentration, the planar carrier density obtained from the Hall measurement was divided by the thickness of the ITiO layer. Table 2 provides a summary of the ITiO material characterization results.

Table 2: ITiO Thin Film Characterization.

Material	Type	Thickness (nm)	Mobility ($cm^2/(V \cdot s)$)	Carrier concentration ($1/cm^2$)*	Carrier concentration ($1/cm^3$)**
ITiO	N	14	62.61	172.42×10^{12}	1.23×10^{20}

* Carrier concentration measurement obtained from hall measurement.
** Calculate carrier concentration per unit volume by dividing the measured planar carrier density by the thickness of the ITiO layer.

IV. C-V and I-V Characterization of the ITiO-gated MOSCAP Si-MRM

Fig. S2(a) illustrates the cross-sectional view of the ITiO-gated MOSCAP Si-MRM. To characterize the electrical properties of the ITiO-gated MOSCAP Si-MRM, the gate bias on ITiO varied while Si was grounded. As depicted in Fig. S2(b), the experimental capacitance of the device was measured as a function of the gate bias. When the device was biased at -1.9 V for modulation, the capacitance was found to be 500 fF. This capacitance corresponds to a dielectric constant (κ) of 12, calculated based on the 62.5% active region of the microring. However, as shown in Fig. S2(a), the device includes a 500 nm wide Si slab attached to the inner ring. Although this slab increases the device's total capacitance, it does not contribute to the effective index modulation, which will be discussed later (Supplementary Information V). To accurately calculate the dynamic power consumption of the ITiO-gated MOSCAP Si-MRM, it is necessary to eliminate such parasitic capacitance. It can be determined by subtracting the contribution of the slab from the total capacitance, resulting in 333 fF. Using the formula ($CV^2/4$), the dynamic power consumption can be further calculated to be 53 fJ/bit. On the other hand, the static power consumption of the ITiO-gated MOSCAP Si-MRM is primarily determined by the leakage current (Fig. S2(c)). When the device is biased at -1.9V, the leakage current is measured to be 495 pA. The E-O tuning efficiency of 117 pm/V is employed to calculate the static power consumption, resulting in a value of 4.27 nW/nm.

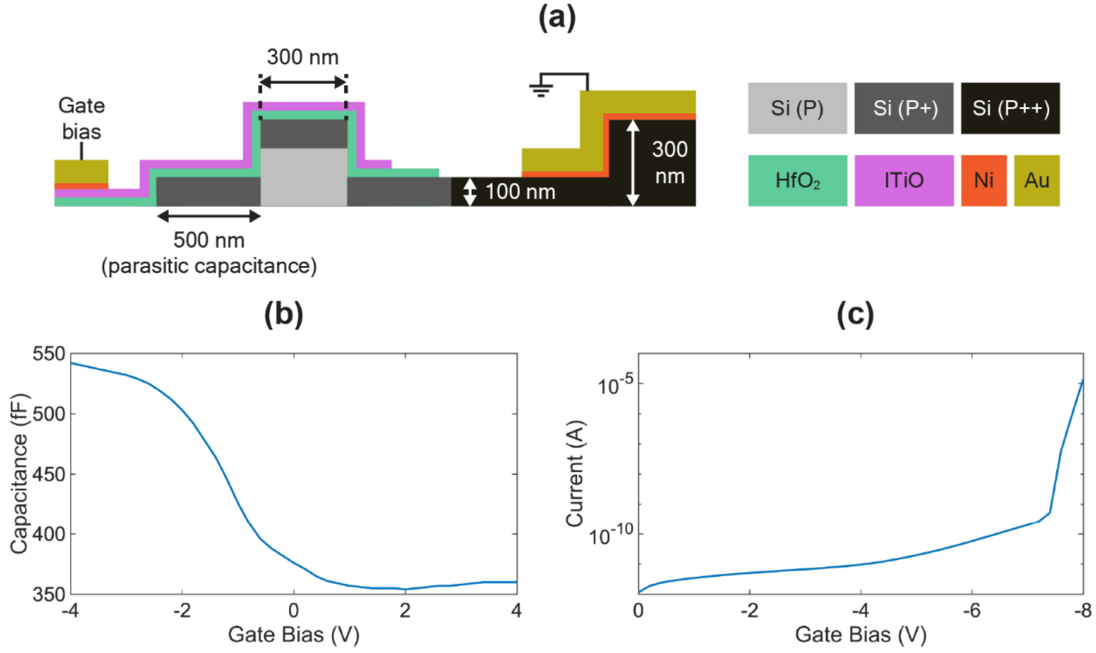

Fig. S2: Electrical characterization of the ITiO-gated MOSCAP Si-MRM with ITiO/HfO2/Si MOSCAP. (a) Cross-sectional view of the ITiO-gated MOSCAP Si-MRM. (b) Capacitance-Voltage (C-V) Curve. (c) Current-Voltage (I-V) Curve.

V. Analysis of Effective Index Modulation Contribution in ITiO-Gated MOSCAP Si-MRM

In Fig. 2(b), the optical mode in the ring waveguide undergoes a shift towards the ring's outer edge due to the bending. This shift leads to varying degrees of overlap between the optical mode and different sides of the ring waveguide, affecting the effective index modulation (Δn_{eff}). To analyze the contributions of each side of the ITiO-gated MOSCAP Si-MRM to Δn_{eff}, the ITiO coverage region is divided into four sections, as shown in Fig. S3(a): (1) the top of the ring, (2) the outer sidewall, (3) the inner sidewall, and (4) the slab. Fig. S3(b) presents a comparison of the simulated effective index modulation per applied bias ($\partial n_{eff}/\partial V$) for each section. Narrowing the waveguide increases the overlap with the sidewalls, leading to a significant $\partial n_{eff}/\partial V$ on both sidewalls (sections 2 and 3). Additionally, due to the optical mode shifting towards the outer edge of the ring, section 2 exhibits a stronger $\partial n_{eff}/\partial V$ compared to section 3. Since the optical mode is primarily confined within the ring, the top of the ring (section 1) still contributes a small extent to $\partial n_{eff}/\partial V$. On the other hand, the contribution of $\partial n_{eff}/\partial V$ from the slab (section 4) is nearly negligible.

While sections 1 and 4 collectively contribute approximately 10% of the total $\partial n_{eff}/\partial V$, they account for 42.9% of the total capacitance. In contrast, sections 2 and 3 contribute about 90% of the total $\partial n_{eff}/\partial V$ while only

contributing 57.1% of the total capacitance. As results, sections 1 and 4, particularly section 4, behave more like parasitic capacitance.

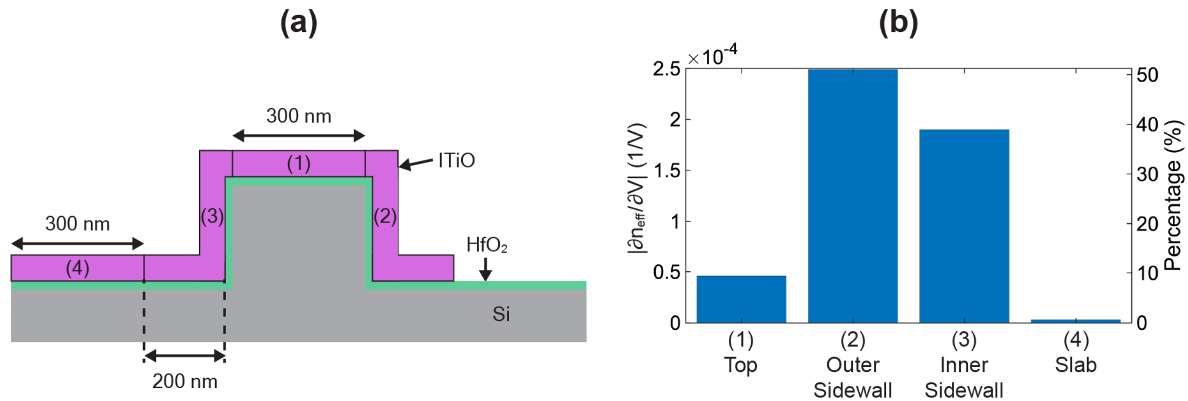

Fig. S3: (a) Illustration for the division of ITiO coverage sections in the MRM waveguide, including (1) the top side of the ring, (2) outer ring sidewall with 200 nm slab, (3) inner ring sidewall with 200 nm slab, and (4) 300 nm slab only. (b) Comparison of simulated effective index modulation per applied bias ($\partial n_{eff}/\partial V$) among the different sections.

References

1. Sakib, M. *et al.* A high-speed micro-ring modulator for next-generation energy-efficient optical networks beyond 100 Gbaud. in *CLEO* SF1C.3 (2021).

2. Zhang, Y. *et al.* 240 Gb/s optical transmission based on an ultrafast silicon microring modulator. *Photonics Res.* **10**, 1127–1133 (2022).

3. Campenhout, J. Van *et al.* Low-voltage, low-loss, multi-Gb/s silicon micro-ring modulator based on a MOS capacitor. in *OFC/NFOEC* 1–3 (2012).

4. Zhang, W. *et al.* Harnessing plasma absorption in silicon MOS ring modulators. *Nat. Photonics* **17**, 273–279 (2023).

5. Liang, D. *et al.* An Energy-Efficient and Bandwidth-Scalable DWDM Heterogeneous Silicon Photonics Integration Platform. *IEEE J. Sel. Top. Quantum Electron.* **28**, 1–19 (2022).

6. Kong, D., Liu, Y., Ding, Y., Hu, H. & Luan, C. *Ultrahigh-modulation-efficiency graphene-silicon micro-ring modulator*. (2023). doi:10.21203/rs.3.rs-2921645/v1.

7. Eppenberger, M. *et al.* Resonant plasmonic micro-racetrack modulators with high bandwidth and high temperature tolerance. *Nat. Photonics* **17**, 360–367 (2023).